A NOVEL SEMI-IMPLICIT PRESSURE-BASED SOLVER FOR LES OF COMPRESSIBLE FLOWS

Radouan Boukharfane
Mohammed VI Polytechnic University (UM6P)
College of Computing, Benguerir, Morocco
radouan.boukharfane@um6p.ma

ABSTRACT

In this work a semi-implicit pressure-based solver for the compressible Navier–Stokes equations, designed to efficiently handle flows across all Mach number regimes, is presented. The method builds upon the characteristic-based fractional-step approach by treating pressure and viscous terms implicitly, while convection is handled explicitly. Unlike traditional formulations based on specific enthalpy, we reformulate the energy equation in terms of total energy, improving consistency in compressible regimes. A Helmholtz equation governs the pressure correction, allowing acoustic effects to propagate at finite speeds and enabling larger time steps than explicit schemes, particularly in low-Mach-number flows. The solver uses a vertex-centered finite-volume discretization with second-order accuracy. Validation is carried out through simulations of supersonic flow over a cylinder and decaying isotropic turbulence at various turbulent Mach numbers. Results show good agreement with reference data, demonstrating the solver's robustness and accuracy in both shock-dominated and weakly compressible flows. This approach offers an efficient and scalable solution for multiscale compressible flow simulations in complex geometries.

INTRODUCTION

The compressible Navier-Stokes equations govern the dynamics of viscous, heat-conducting fluids, serving as a cornerstone for numerous engineering applications, such as aerospace propulsion and wind energy systems. Expressed as a system of hyperbolic partial differential equations (PDEs), these equations enforce the conservation of mass, momentum, and energy. In the inviscid, non-diffusive limit, they simplify to the Euler equations, whereas at low Mach numbers—defined as the ratio of flow velocity to sound speed—they transition to the incompressible Navier-Stokes equations. The Mach number dictates the flow regime, posing substantial computational challenges in numerical simulations where high-speed compressible effects and low-speed hydrodynamic behavior coexist within a single domain.

A primary numerical bottleneck stems from the acoustic Courant-Friedrichs-Lewy (CFL) condition when explicit solvers are employed. In practical scenarios—such as low-Mach-number flows near injectors or transitional compressible flows—the time step is constrained by the acoustic CFL limit rather than the convective CFL limit, rendering simulations computationally prohibitive. For example, at a Mach number of 0.1, the acoustic time step restriction is roughly an order of magnitude more stringent than its convective counterpart, dramatically escalating computational expense. This challenge is especially pronounced in simulations requiring extended integration periods, such as those analyzing turbulence statistics or combustion instabilities.

To address this limitation, semi-implicit schemes have emerged to decouple acoustic waves from convective dynamics, enabling larger time steps. Among these, implicit-explicit (IMEX) methods have garnered significant attention (Boscheri & Pareschi, 2021). These techniques leverage flux-splitting strategies (Toro & Vázquez-Cendón, 2012), partitioning the governing equations into an advection system, treated explicitly, and a pressure system, solved implicitly. This separation eliminates the restrictive acoustic CFL constraint, rendering IMEX schemes well-suited for flows spanning all Mach numbers. A parallel approach is found in pressure-based semi-implicit solvers, such as the fractional-step method with characteristic splitting proposed by Moureau *et al.* (2007). This method involves two core steps: an advection step, where flow transport is computed explicitly or implicitly, and a pressure-correction step, where the Helmholtz equation is solved implicitly to capture pressure fluctuations. Unlike traditional Poisson-based solvers, this framework allows pressure perturbations to propagate at finite acoustic speeds, preserving the critical interplay between heat release and acoustic waves.

Building on these advancements, the present study introduces a semi-implicit, pressure-based solver for the compressible Navier–Stokes equations that follows a characteristic-based fractional-step strategy, while adopting a different formulation of the energy equation compared to earlier approaches. In contrast to the method of Moureau *et al.* (2007), which is based on a specific enthalpy formulation, the present solver is written directly in terms of the *total energy*. Although the present work is restricted to single-species flows, this choice simplifies the mathematical structure of the method by avoiding additional thermodynamic coupling terms inherent to enthalpy-based formulations. Using total energy as the primary thermodynamic variable provides a fully conservative framework that remains valid across all Mach number regimes and leads to a more compact and transparent formulation of the pressure-correction step. In particular, the derivation of the Helmholtz equation governing the pressure correction is simplified, as pressure work and kinetic energy contributions are treated in a unified manner within the total-energy balance. From a numerical perspective, the proposed solver treats pressure and viscous terms implicitly while handling convective transport explicitly, thereby alleviating the stringent time-step restrictions imposed by acoustic and viscous stability constraints. While the present study focuses on single-species viscous flows, the total-energy formulation adopted here provides a natural and robust foundation for future extensions. The capabilities and accuracy of the method are demonstrated through two- and three-dimensional simulations of supersonic flows and decaying compressible turbulence, illustrating its effectiveness across a wide range of flow regimes.

1 Development of the Characteristic–based Fractional–step Method

The present simulations are performed using a pressure-based semi-implicit solver for the compressible Navier–Stokes equations, written in conservative form for mass, momentum, and total energy:

$$\begin{aligned} \frac{\partial \rho}{\partial t}+\frac{\partial(\rho u_i)}{\partial x_i}&=0,\\ \frac{\partial(\rho u_i)}{\partial t}+\frac{\partial(\rho u_i u_j)}{\partial x_j}-\frac{\partial \tau_{ij}}{\partial x_j}+\frac{\partial p}{\partial x_i}&=0,\\ \frac{\partial(\rho e)}{\partial t}+\frac{\partial(\rho e u_i)}{\partial x_i}+\frac{\partial(p u_i)}{\partial x_i}-\frac{\partial(u_j\tau_{ij})}{\partial x_i}+\frac{\partial q_i}{\partial x_i}&=0, \end{aligned} \tag{1}$$

where ρ is the density, u_i the velocity components, p the pressure, $e=e_{\text{int}}+\frac{1}{2}u_k u_k$ the total specific energy (internal energy plus kinetic energy), τ_{ij} the viscous stress tensor, and q_i the heat flux. The viscous stress tensor for a Newtonian fluid is $\tau_{ij}=\mu\left(\frac{\partial u_i}{\partial x_j}+\frac{\partial u_j}{\partial x_i}\right)-\frac{2}{3}\mu\,\delta_{ij}\frac{\partial u_k}{\partial x_k}$, where μ is the dynamic viscosity and δ_{ij} is the Kronecker delta. The heat flux follows Fourier's law, $q_i=-\kappa\,\partial T/\partial x_i$, with κ the thermal conductivity. Thermodynamic closure is provided by the calorically perfect gas equation of state $p=\rho RT=(\gamma-1)\rho e_{\text{int}}$, where R is the specific gas constant, T the temperature, and $\gamma=c_p/c_v$ the ratio of specific heats. The local speed of sound is $c=\sqrt{\gamma p/\rho}$. In low-Mach-number compressible flows, the dynamics are governed by strongly separated time scales associated with convective transport and acoustic propagation. This separation can be formally identified by considering the eigenvalues of the one-dimensional inviscid flux Jacobian,

$$\lambda=u-c,\quad u,\quad u+c, \tag{2}$$

corresponding respectively to acoustic and convective modes. Following the characteristic-based approach,

$$\begin{pmatrix}u+c\\u-c\\u\end{pmatrix}=\begin{pmatrix}u\\u\\u\end{pmatrix}+\begin{pmatrix}c\\-c\\0\end{pmatrix}, \tag{3}$$

thereby enabling an explicit separation between transport phenomena occurring at the flow velocity and compressibility effects associated with pressure waves. This decomposition is extended to the full three-dimensional compressible Navier–Stokes equations through a fractional-step procedure, in which the governing equations are split into an advective subsystem and an acoustic subsystem.

Advective subsystem The advective step is constructed by isolating the transport terms and removing all contributions proportional to the velocity divergence, which are associated with acoustic compression and expansion. Writing

$$\frac{\partial(\rho u_i)}{\partial x_i}=u_i\frac{\partial \rho}{\partial x_i}+\rho\frac{\partial u_i}{\partial x_i},$$

the second term is identified as purely acoustic and is therefore excluded from the advective update. Applying the same procedure to momentum and total energy leads to

$$\begin{aligned} \frac{\rho^*-\rho}{\Delta t}+\frac{\partial(\rho u_i)}{\partial x_i}-\rho\frac{\partial u_i}{\partial x_i}&=0,\\ \frac{(\rho u_i)^*-(\rho u_i)}{\Delta t}+\frac{\partial(\rho u_i u_j)}{\partial x_j}-\rho u_i\frac{\partial u_j}{\partial x_j}-\frac{\partial \tau_{ij}}{\partial x_j}&=0,\\ \frac{(\rho e)^*-(\rho e)}{\Delta t}+\frac{\partial(\rho e u_i)}{\partial x_i}-\rho e\frac{\partial u_i}{\partial x_i}-\frac{\partial(u_j\tau_{ij})}{\partial x_i}+\frac{\partial q_i}{\partial x_i}&=0. \end{aligned} \tag{4}$$

Acoustic subsystem and pressure correction The acoustic step restores compressibility by reintroducing the effects of velocity divergence and pressure gradients:

$$\begin{aligned} \frac{\rho^{n+1}-\rho^*}{\Delta t}+\rho\frac{\partial u_i}{\partial x_i}&=0,\\ \frac{(\rho u_i)^{n+1}-(\rho u_i)^*}{\Delta t}+\rho u_i\frac{\partial u_j}{\partial x_j}+\frac{\partial p}{\partial x_i}&=0,\\ \frac{(\rho e)^{n+1}-(\rho e)^*}{\Delta t}+\rho e\frac{\partial u_i}{\partial x_i}+\frac{\partial(u_i p)}{\partial x_i}&=0. \end{aligned} \tag{5}$$

Introducing the pressure correction $\delta p=p^{n+1}-p^*$ and linearizing the thermodynamic relation at constant entropy yield $\delta p=c^2\delta\rho$, or, in discrete form $\frac{\delta p}{\Delta t}=-c^2\rho\frac{\partial u_i}{\partial x_i}$. Substitution leads to

$$\begin{aligned} \frac{\rho^{n+1}-\rho^*}{\Delta t}-\frac{1}{c^2}\frac{\delta p}{\Delta t}&=0,\\ \frac{(\rho u_i)^{n+1}-(\rho u_i)^*}{\Delta t}-\frac{u_i}{c^2}\frac{\delta p}{\Delta t}+\frac{\partial}{\partial x_i}\left(\frac{p^*+p^{n+1}}{2}\right)&=0,\\ \frac{(\rho e)^{n+1}-(\rho e)^*}{\Delta t}-\frac{e}{c^2}\frac{\delta p}{\Delta t}+\frac{\partial}{\partial x_i}\left(\frac{u_i p^*+u_i p^{n+1}}{2}\right)&=0. \end{aligned} \tag{6}$$

Helmholtz pressure equation Taking the divergence of the momentum equation yields the Helmholtz problem

$$\underbrace{\frac{\partial^2\delta p}{\partial x_i\partial x_i}}_{\text{pressure propagation}}-\underbrace{\frac{\partial}{\partial x_i}\left(\frac{2u_i}{\Delta t c^2}\delta p\right)}_{\text{acoustic convection}}-\underbrace{\frac{4}{c^2\Delta t^2}\delta p}_{\text{low-Mach stabilization}}=\mathscr{H}, \tag{7}$$

with

$$\mathscr{H}=-2\frac{\partial^2 p^*}{\partial x_i\partial x_i}+\frac{4}{\Delta t}\left[\frac{\rho^*-\rho}{\Delta t}+\frac{\partial}{\partial x_i}\left(\frac{(\rho u_i)^*+(\rho u_i)}{2}\right)\right]. \tag{8}$$

Here $\mathscr{H}$ depends only on quantities available from the advective step and the previous time level, so equation (7) is a closed elliptic problem for the single unknown δp. Equation (7) is of Helmholtz type and represents an implicit treatment of acoustic phenomena. The Laplacian term accounts for the global propagation of pressure disturbances, while the zeroth-order term proportional to δp ensures numerical stability in the low-Mach-number limit. The additional convective contribution arises from the consistent treatment of acoustic transport in a moving medium. The Helmholtz equation is solved using a BiCGStab iterative solver preconditioned by a Jacobi scheme. Once δp is obtained, all conservative variables are updated according to (6), yielding a fully compressible, conservative, and stable time advancement.

Time-step selection Since pressure and viscous terms are treated implicitly, the time step Δt is constrained only by the convective CFL condition $\Delta t = \mathrm{CFL}\,\frac{h}{\|u\|_\infty}$, where h is the characteristic mesh spacing and $\mathrm{CFL} \leq 1$ is the Courant number. In contrast to fully explicit compressible solvers, the acoustic CFL constraint $\Delta t \leq h/c$ is circumvented, yielding a speed-up factor of approximately $1/\mathrm{Ma}$ at low Mach numbers. In the present simulations $\mathrm{CFL} = 0.5$ is used throughout.

Low-Mach-number asymptotics The consistency of the present characteristic-based fractional-step method in the low-Mach-number limit may be examined by considering the asymptotic behaviour of the acoustic correction as $\mathrm{Ma} \to 0$. Introducing the classical low-Mach scaling (Majda & Sethian, 1985; Klein, 1995),

$$p = p_0 + \mathrm{Ma}^2 p_1, \qquad \mathbf{u} = \mathcal{O}(1), \qquad \rho = \rho_0 + \mathcal{O}(\mathrm{Ma}^2),$$

where p_0 is the leading-order thermodynamic pressure, spatially uniform at leading order and determined by the global thermodynamic state, p_1 is the hydrodynamic pressure correction that drives the flow and appears at order Ma^2, and ρ_0 is the leading-order density satisfying $p_0 = \rho_0 R T_0$. It follows that pressure fluctuations associated with acoustic waves scale as $\mathcal{O}(\mathrm{Ma}^2)$, while the leading-order pressure p_0 acts as a Lagrange multiplier enforcing the leading-order divergence-free constraint on the velocity field. Under this scaling, the pressure correction δp remains of order $\mathcal{O}(\mathrm{Ma}^2)$, whereas the coefficient $1/c^2$ scales as $\mathcal{O}(\mathrm{Ma}^2)$. Consequently, the zeroth-order term in the Helmholtz equation $\frac{4}{c^2 \Delta t^2}\,\delta p$, remains finite as $\mathrm{Ma} \to 0$, ensuring the well-posedness of the elliptic pressure problem and preventing the stiffness typically encountered in fully explicit compressible formulations. In this asymptotic limit, the Helmholtz equation smoothly degenerates into a Poisson-type equation for the pressure correction, and the acoustic step reduces to a projection enforcing a divergence-free velocity field at leading order. The resulting scheme therefore recovers the classical incompressible pressure-projection method, while retaining a fully conservative formulation for mass, momentum, and total energy at finite Mach numbers. Importantly, no artificial low-Mach correction or pressure rescaling is required, as the asymptotic consistency is ensured by the characteristic-based splitting and the implicit treatment of acoustic terms. The method thus provides a unified framework valid across a wide range of Mach numbers, from nearly incompressible to moderately compressible regimes.

Entropy consistency The entropy behaviour of the present characteristic-based fractional-step method may be examined by considering the evolution of the specific entropy $s(\rho, e)$, defined through the thermodynamic relation $T\,\mathrm{d}s = \mathrm{d}e - \frac{p}{\rho^2}\,\mathrm{d}\rho$, where T denotes the temperature. In the continuous inviscid limit, combining the conservation equations for mass, momentum, and total energy yields the entropy transport equation

$$\frac{\partial(\rho s)}{\partial t} + \frac{\partial(\rho s u_i)}{\partial x_i} = 0, \tag{9}$$

indicating that entropy is conserved along fluid trajectories in the absence of viscous dissipation and heat conduction. Within the present fractional-step formulation, this entropy transport property can be analysed by examining the two substeps separately. During the advective step, the governing equations reduce to pure convective transport along the velocity field, with all pressure-related and dilatational contributions removed. As a consequence, the entropy equation reduces to

$$\frac{\rho^* s^* - \rho s}{\Delta t} + \frac{\partial(\rho s u_i)}{\partial x_i} - \rho s \frac{\partial u_i}{\partial x_i} = 0, \tag{10}$$

which is a consistent discrete approximation of the convective entropy transport equation. During the acoustic step, entropy variations arise solely from reversible compression and expansion. Introducing the pressure correction δp and using the linearized thermodynamic relation $\delta p = c^2 \delta\rho$, the corresponding entropy variation satisfies

$$T\,\delta s = \delta e - \frac{p}{\rho^2}\,\delta\rho = \mathcal{O}(\delta p^2), \tag{11}$$

indicating that the acoustic correction does not generate entropy at leading order. Consequently, the pressure correction step is entropy-neutral to first order and merely redistributes energy between kinetic and internal modes. At the discrete level, entropy production is therefore exclusively associated with viscous dissipation and thermal diffusion, consistently with the continuous compressible Navier–Stokes equations. No additional entropy generation is introduced by the characteristic-based splitting itself, ensuring that the method remains thermodynamically consistent, particularly in the low-Mach-number regime where spurious entropy errors may otherwise dominate.

Spatial discretization The spatial discretization relies on a vertex-centered finite-volume formulation. Control volumes are constructed as median dual cells surrounding each mesh node, formed by assembling subtriangles in two dimensions or subtetrahedra in three dimensions. Volume integrals are evaluated using a second-order Taylor expansion about the cell centroid. Convective fluxes at control-volume faces are reconstructed using a linear (MUSCL-type) interpolation with a slope limiter to suppress spurious oscillations near shocks; in the present implementation a Barth–Jespersen limiter is employed. Viscous and heat-flux terms are discretized using a centered second-order approximation of the gradients, computed via the Green–Gauss theorem on the dual cells. This approach ensures strict conservation of mass, momentum, and energy while preserving second-order spatial accuracy on both structured and unstructured meshes.

2 Navier–Stokes characteristic boundary conditions

Accurate boundary conditions are essential for low-Mach-number compressible flows, as spurious reflections of acoustic waves may severely contaminate the solution in the interior of the domain. In the present work, boundary conditions are imposed using the Navier–Stokes Characteristic Boundary Condition (NSCBC) methodology, originally introduced for compressible flows and here adapted consistently to the characteristic-based fractional-step framework described in §1. The NSCBC approach relies on a characteristic decomposition of the governing equations normal to the boundary, allowing incoming and outgoing wave contributions to be treated separately. This formulation is particularly well suited to the present solver, as both the interior scheme and the boundary treatment are based on an explicit separation between convective and acoustic phenomena.

Local one-dimensional inviscid formulation At a boundary face, the flow is locally assumed to be one-dimensional and inviscid in the direction normal to the boundary. Introducing a local orthonormal frame (e_1, e_2, e_3), with e_1 aligned with the outward normal, the compressible Navier–Stokes equations are locally reduced to a Local One-Dimensional Inviscid (LODI) system. For a perfect gas and neglecting viscous and diffusive source terms, the LODI system written in primitive variables reads

$$
\begin{aligned}
\frac{\partial \rho}{\partial t} + \frac{1}{c^2}\left(L_s + \frac{1}{2}(L_p + L_m)\right) &= 0,\\
\frac{\partial u_1}{\partial t} + \frac{1}{2\rho c}(L_p - L_m) &= 0,\\
\frac{\partial u_2}{\partial t} + L_{t1} &= 0,\\
\frac{\partial u_3}{\partial t} + L_{t2} &= 0,\\
\frac{\partial p}{\partial t} + \frac{1}{2}(L_p + L_m) &= 0,
\end{aligned}
\tag{12}
$$

where c denotes the local speed of sound and the quantities L_i represent the amplitudes of characteristic waves propagating normal to the boundary. The characteristic wave amplitudes are defined as

$$
\begin{aligned}
L_s &= c^2 \frac{\partial \rho}{\partial e_1} - \frac{\partial p}{\partial e_1},\\
L_p &= \frac{\partial p}{\partial e_1} + \rho c \frac{\partial u_1}{\partial e_1},\\
L_m &= \frac{\partial p}{\partial e_1} - \rho c \frac{\partial u_1}{\partial e_1},\\
L_{t1} &= \rho c \frac{\partial u_2}{\partial e_1},\\
L_{t2} &= \rho c \frac{\partial u_3}{\partial e_1}.
\end{aligned}
\tag{13}
$$

The eigenvalues associated with these waves are $u_1 - c$, u_1, and $u_1 + c$, corresponding respectively to incoming acoustic, convective, and outgoing acoustic modes, depending on the flow direction and boundary type.

Coupling with the fractional-step formulation In the present solver, the interior time integration separates advective and acoustic effects through a fractional-step procedure. The NSCBC formulation is made consistent with this approach by applying characteristic boundary conditions exclusively to the acoustic contribution, while convective transport is handled explicitly by the advective step. At each time step, boundary conditions are enforced by prescribing the amplitudes of incoming characteristic waves, while outgoing waves are extrapolated from the interior solution. This procedure ensures that acoustic information is allowed to leave the domain without reflection, while only physically admissible information is imposed at the boundary.

Subsonic inflow boundary conditions For a subsonic inflow, one acoustic wave enters the domain, while the remaining waves are outgoing. The incoming characteristic amplitudes are prescribed using a relaxation strategy toward reference inflow values:

$$
\begin{aligned}
L_m &= -\sigma_u \rho c (u_1 - u_{1,\mathrm{ref}}),\\
L_{t1} &= -\sigma_t \rho c (u_2 - u_{2,\mathrm{ref}}),\\
L_{t2} &= -\sigma_t \rho c (u_3 - u_{3,\mathrm{ref}}),\\
L_s &= -\sigma_T \rho \gamma R (T - T_{\mathrm{ref}}),
\end{aligned}
\tag{14}
$$

where σ_u, σ_t, and σ_T are relaxation coefficients controlling the strength of the boundary forcing. This formulation enforces velocity and temperature weakly while allowing pressure to adjust dynamically, ensuring compatibility with the low-Mach-number acoustic behaviour of the flow.

Subsonic outflow boundary conditions For a subsonic outflow, a single acoustic wave enters the domain. To avoid artificial reflections, this incoming wave is prescribed using a pressure relaxation $L_m = \sigma_p \rho c (p - p_{\mathrm{ref}})$, where p_{ref} is the target static pressure at the outlet and σ_p is a relaxation parameter. All other characteristic waves are extrapolated from the interior solution, allowing vortical and acoustic structures to leave the domain with minimal distortion.

Consistency with low-Mach asymptotics The present NSCBC implementation is asymptotically consistent with the low-Mach-number limit. As pressure fluctuations scale as $\mathcal{O}(\mathrm{Ma}^2)$, the characteristic formulation ensures that pressure acts as a Lagrange multiplier enforcing mass conservation, while acoustic perturbations are correctly damped at open boundaries. Combined with the Helmholtz-based pressure correction in the interior, this yields a globally consistent treatment of acoustic waves across both interior and boundary regions. The NSCBC formulation therefore provides a physically consistent and numerically robust boundary treatment fully aligned with the characteristic-based fractional-step method, enabling accurate simulations of low-Mach-number compressible flows without spurious boundary reflections.

3 RESULTS AND DISCUSSION

3.1 Supersonic flow over a circular cylinder

A first validation test case consists of a two-dimensional supersonic flow over a circular cylinder. This configuration is a classical benchmark for compressible solvers, as it simultaneously involves strong shock waves, boundary-layer development, and shock–wake interactions. Two freestream Mach numbers are considered, $M_\infty = 2.0$ and $M_\infty = 3.0$, allowing the solver to be assessed over a range of supersonic regimes. The computational domain extends over $L_x = 7d$ in the streamwise direction and $L_y = 18d$ in the transverse direction, where d denotes the cylinder diameter. These domain dimensions were selected to ensure that the detached bow shock remains fully contained within the computational domain and that acoustic or shock reflections from the boundaries do not contaminate the near-wake region. The cylinder is placed sufficiently far from the inlet to allow the bow shock to develop naturally. The simulations are performed at a Reynolds number based on the cylinder diameter $\mathrm{Re}_d = \frac{\rho_\infty U_\infty d}{\mu_\infty} = 5.5 \times 10^5$, which corresponds to the conditions investigated numerically by Li *et al.* (2013). The freestream velocity is related to the Mach number through $M_\infty = \frac{U_\infty}{a_\infty}$, and $a_\infty = \sqrt{\gamma \frac{p_\infty}{\rho_\infty}}$, where a_∞ denotes the speed of sound in the undisturbed flow. A body-fitted mesh is employed, with local refinements in the vicinity of the cylinder wall, the bow shock, and the downstream wake. Particular attention is paid to the near-wall resolution, with a nondimensional wall distance maintained below $y^+ < 1$ throughout the domain, ensuring an accurate representation of the viscous boundary layer. This resolution is essential for capturing the interaction between the detached shock and the boundary layer, which directly affects the pressure distribution along the cylinder surface. Figure 1 shows an instantaneous snapshot of the transverse velocity component u_2 for the inviscid Mach 3 case. The bow shock is clearly visible upstream of the cylinder, together with the shear layers developing along the cylinder sides and the wake structure downstream. The ability of the solver to sharply capture the shock while maintaining smooth flow features in the wake illustrates the effectiveness of the shock-capturing and characteristic-based treatment. To further quantify the solver accuracy, the surface pressure distribution is examined through the pressure coefficient $C_p(\theta) = \frac{p(\theta)-p_\infty}{\frac{1}{2}\rho_\infty U_\infty^2}$, where θ denotes the azimuthal angle measured from the upstream stagnation point. In supersonic flow, the pressure coefficient exhibits a sharp peak near the stagnation point due to the bow shock, followed by a rapid decrease along the cylinder surface as the flow accelerates. Figure 2 compares the computed pressure coefficient distributions for $\mathrm{Ma}_\infty = 2.0$ and $\mathrm{Ma}_\infty = 3.0$ with the numerical results reported by Li *et al.* (2013). In both cases, the present solver reproduces the correct pressure levels at the stagnation point, as well as the overall shape of the C_p distribution along the cylinder surface. The agreement remains excellent over the entire circumference, including the region downstream of the shock where strong pressure gradients are present. These results demonstrate that the solver accurately captures the essential physical mechanisms governing supersonic flow over bluff bodies, including shock formation, shock–boundary-layer interaction, and wake development. This test case therefore provides a robust validation of the compressible formulation and the numerical methods employed before proceeding to more complex configurations.

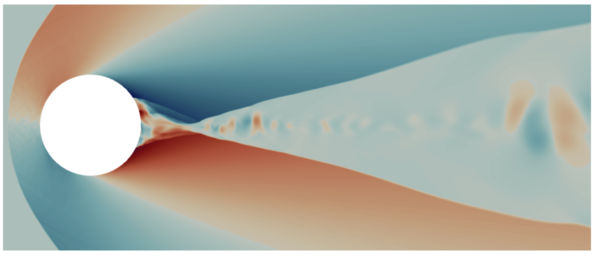

Figure 1: Instantaneous u_2 velocity field for Mach 3 supersonic inviscid flow over a 2D circular cylinder

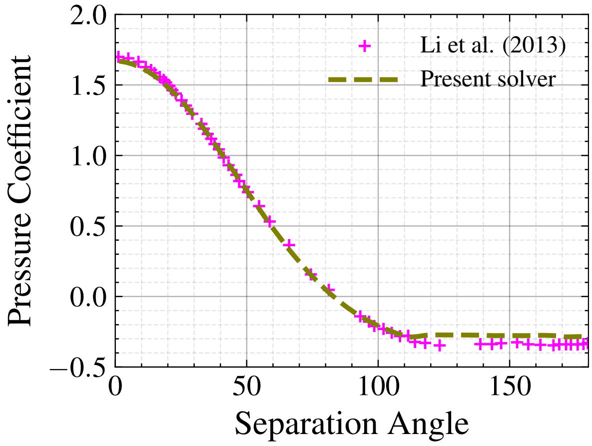

(a) Ma = 2.0.

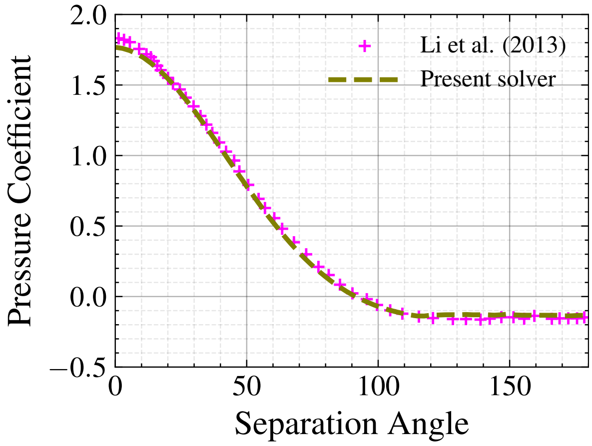

(b) Ma = 3.0.

Figure 2: Comparisons between simulated surface pressure coefficients

3.2 Shock interaction with a circular cylinder

The interaction of a moving planar shock wave with a circular cylinder, commonly referred to as the *Schardin problem* Schardin (1957); Boukharfane (2018), is considered here as a stringent validation test for the present compressible solver. This configuration involves the simultaneous occurrence of strong shock waves, shock diffraction, shock reflection, and vortex generation, and has therefore been extensively investigated in experimental, analytical, and numerical studies. In this test case, an initially planar shock wave propagates through a quiescent medium and impinges on a stationary circular cylinder. The shock is initialized upstream of the cylinder and propagates at a constant speed corresponding to an incident shock Mach number $\mathrm{Ma}_s = \frac{U_s}{a_0} = 2.81$, where U_s denotes the shock propagation speed and a_0 is the speed of sound in the undisturbed medium ahead of the shock. The pre-shock flow is initially at rest, while the post-shock conditions are prescribed consistently with the Rankine–Hugoniot relations for a normal shock. The computational domain and mesh characteristics are identical to those employed in the preceding moving-shock benchmark cases, ensuring a consistent level of spatial resolution. The cylinder is positioned sufficiently far from the inlet boundary so that the shock remains planar prior to the interaction. Symmetry with respect to the centerline is exploited to reduce the computational cost, and NSCBC boundary conditions are applied to allow outgoing acoustic and shock waves to leave the domain without spurious reflections. As the shock impinges on the cylinder, a complex wave interaction system develops. The initially planar shock diffracts around the cylinder, giving rise to a curved reflected shock and a transmitted shock propagating downstream. Simultaneously, the interaction generates a pair of triple points associated with the intersection of the incident shock, the reflected shock, and the slip lines. The trajectories of the upper and lower triple points are tracked over time and constitute a sensitive quantitative diagnostic of the shock–body interaction.

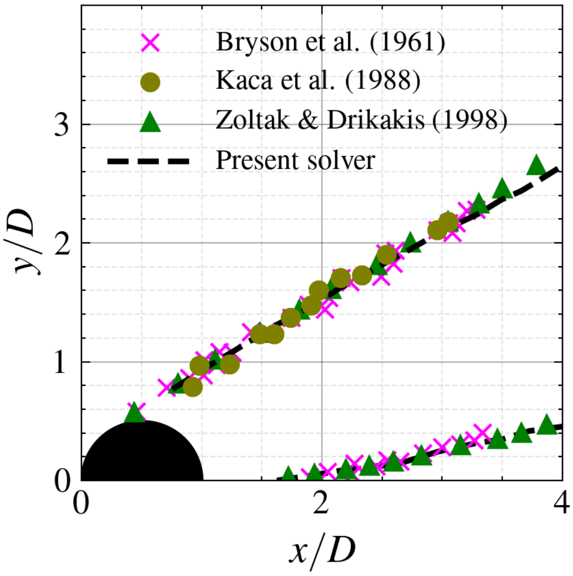

Figure 3: Trajectories of the two triple points for the planar shock–cylinder interaction in the Schardin problem.

The computed trajectories of the two triple points are shown in Fig. 3. The present results are in close agreement with both numerical simulations reported in the literature and available experimental measurements (e.g. Bryson & Gross (1961); Zółtak & Drikakis (1998); Kaca (1988)), confirming that the solver accurately captures shock diffraction and reflection processes as well as the associated slip-line dynamics. Further insight into the flow physics is provided by instantaneous flow visualizations. Figure 4 shows the instantaneous density field during the interaction. The curved reflected shock and the Mach stem forming near the cylinder surface are clearly visible. In addition, the formation of a counter-rotating vortex pair in the wake of the cylinder is observed, resulting from baroclinic vorticity production induced by the misalignment of pressure and density gradients across the shock.

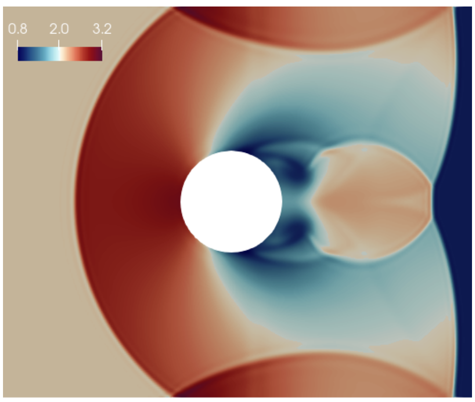

Figure 4: Instantaneous density field for the Schardin problem.

3.3 Decaying compressible isotropic turbulence

The decay of homogeneous isotropic turbulence (HIT) is considered as a second validation test case to assess the accuracy and robustness of the present semi-implicit, pressure-based compressible solver across different compressibility regimes. This configuration provides a stringent test of the numerical method, as it involves the interaction between nonlinear turbulence dynamics and compressibility effects in the absence of mean flow and boundaries. The simulations are performed for two initial turbulent Mach numbers $\mathrm{Ma}_t = \frac{u'_{\mathrm{rms}}}{a_0}$, namely $\mathrm{Ma}_t = 0.1$, representative of the near-incompressible regime, and $\mathrm{Ma}_t = 0.5$, corresponding to a nonlinear subsonic compressible regime. Here, u'_{rms} denotes the root-mean-square velocity fluctuation and a_0 is the initial speed of sound. In both cases, the Taylor-scale Reynolds number is set to $\mathrm{Re}_\lambda = \frac{u'_{\mathrm{rms}}\lambda}{\nu} = 72$, where λ is the Taylor microscale and ν the kinematic viscosity. The flow is simulated in a cubic, triply periodic domain of size $[0, 2\pi]^3$, ensuring statistical homogeneity and isotropy throughout the evolution. Periodic boundary conditions are applied in all three spatial directions, and no mean flow is imposed. The numerical resolution consists of 64^3 grid points, consistent with the reference simulations of Samtaney *et al.* (2001). A Smagorinsky subgrid-scale model with coefficient $C_s = 0.1$ is employed to account for unresolved scales, yielding a large-eddy simulation framework comparable to the original study. The subgrid-scale viscosity is $\mu_{\mathrm{sgs}} = (C_s\Delta)^2|\bar{S}|$, where Δ is the filter width (taken as the local mesh spacing) and $|\bar{S}| = (2\bar{S}_{ij}\bar{S}_{ij})^{1/2}$ is the magnitude of the resolved strain-rate tensor. The initial velocity field is divergence-free and constructed to satisfy a prescribed isotropic energy spectrum $E(k) = A_0 k^4 \exp\left(-\frac{2k^2}{k_0^2}\right)$, where k is the wavenumber, k_0 denotes the peak wavenumber of the spectrum, and A_0 is a normalization constant chosen to match the desired initial turbulent kinetic energy. In the present simulations, $k_0 = 8$ and $A_0 = 1.3 \times 10^{-4}$. This spectral shape ensures that the initial energy is concentrated at large scales while remaining sufficiently smooth to avoid spurious numerical transients. The temporal evolution of the resolved turbulent kinetic energy $\mathscr{E}_K(t) = \frac{1}{2}\langle \rho u_i u_i\rangle$, where $\langle\cdot\rangle$ denotes a volume average over the computational domain, is used as the primary diagnostic to evaluate the turbulence decay. Figure 5 show the time evolution of $\mathscr{E}_K$ for $\mathrm{Ma}_t = 0.1$ and $\mathrm{Ma}_t = 0.5$, respectively.

For both Mach numbers, the present solver reproduces the expected monotonic decay of kinetic energy associated with the turbulent cascade and viscous dissipation. Minor discrepancies are observed at early times, which can be attributed to initialization effects and the adjustment of the pressure field during the initial transient. Beyond this initial phase, the decay rates and overall energy levels are in good agreement with the direct numerical simulation results reported by Samtaney *et al.* (2001). The agreement observed in both the near-incompressible and compressible regimes demonstrates that the present semi-implicit formulation accurately captures the coupled evolution of velocity, density, and pressure fluctuations in decaying compressible turbulence. This test case therefore provides a strong validation of the solver's ability to handle compressibility effects in unsteady turbulent flows while preserving the correct kinetic energy decay behavior.

CONCLUSION

A semi-implicit, pressure-based solver for the compressible Navier–Stokes equations has been presented, with the objective of providing a unified and efficient numerical frame-

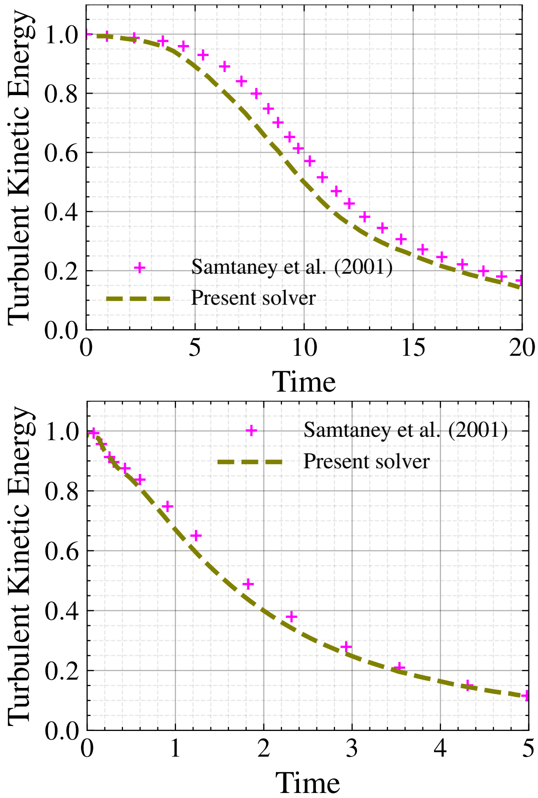

Figure 5: Time evolution of the total volume-averaged kinetic energy of HIT simulation for (top) $\mathrm{Ma}_t = 0.1$ and (bottom) $\mathrm{Ma}_t = 0.5$.

work for flows spanning a wide range of Mach numbers. The method builds upon a characteristic-based fractional-step formulation, in which convective transport is treated explicitly while pressure and viscous effects are handled implicitly. A key feature of the proposed approach is the use of total energy as the primary thermodynamic variable, ensuring consistency in both low- and finite-Mach-number regimes.

The resulting pressure correction leads to a Helmholtz-type equation, allowing acoustic effects to propagate at finite speeds while alleviating the restrictive acoustic CFL constraint inherent to fully explicit compressible solvers. A detailed mathematical analysis demonstrates that the formulation is asymptotically consistent with the incompressible limit, naturally recovering a pressure-projection method as the Mach number tends to zero, without requiring artificial pressure rescaling or ad hoc low-Mach corrections. The entropy analysis further shows that the characteristic-based splitting is thermodynamically consistent, with no spurious entropy production introduced by the pressure correction step. Boundary conditions are imposed using a Navier–Stokes characteristic boundary condition (NSCBC) framework, carefully adapted to the fractional-step methodology. This ensures a consistent treatment of acoustic and convective phenomena at open boundaries, preventing unphysical reflections and preserving the correct low-Mach asymptotic behaviour of the coupled interior–boundary system. The solver has been validated against a set of representative and demanding test cases, including supersonic flow over a circular cylinder, the Schardin shock–cylinder interaction problem, and decaying compressible isotropic turbulence at different turbulent Mach numbers. In all cases, the numerical results show excellent agreement with reference numerical and experimental data, demonstrating the ability of the method to accurately capture shock waves, shock–boundary interactions, and unsteady compressible turbulence across both shock-dominated and weakly compressible regimes.

Overall, the present work provides a robust and scalable numerical framework for multiscale compressible flow simulations in complex geometries. By combining a characteristic-based fractional-step formulation with a total-energy-based semi-implicit treatment of pressure and viscous effects, the method offers a unified and physically consistent description of both low- and high-Mach-number dynamics within a single solver. This makes the approach particularly well suited for applications involving strong spatial or temporal variations in compressibility, such as aeroacoustics, shock–turbulence interactions, and transitional compressible flows. While the present study is restricted to single-species viscous flows, the adoption of a total-energy formulation significantly simplifies the mathematical structure of the method and provides a solid foundation for future developments. In particular, this choice is expected to facilitate extensions to more complex physical models, including multi-species transport, chemical reactions, and coupled multiphysics problems, which will be the focus of future work.

REFERENCES

Boscheri, W. & Pareschi, L. 2021 High order pressure-based semi-implicit IMEX schemes for the 3D Navier-Stokes equations at all Mach numbers. *Journal of Computational Physics* **434**, 110206.

Boukharfane, R. 2018 Contribution à la simulation numérique d'écoulements turbulents compressibles canoniques. PhD thesis, ISAE-ENSMA.

Bryson, A. E. & Gross, R. W. F. 1961 Diffraction of strong shocks by cones, cylinders, and spheres. *Journal of Fluid Mechanics* **10**, 1–16.

Kaca, J. 1988 An interferometric investigation of the diffraction of a planar shock wave over a semicircular cylinder. *NASA STI/Recon Technical Report N* **89**.

Klein, R. 1995 Semi-implicit extension of a Godunov-type scheme based on low mach number asymptotics i: One-dimensional flow. *Journal of Computational Physics* **121** (2), 213–237.

Li, X., Hu, Z., Teng, H. & Jiang, Z. 2013 Numerical simulation of supersonic cylinder wake and its stability. In *Advances in High-Temperature Gas Dynamics Research*, pp. 179–184.

Majda, A. & Sethian, J. 1985 The derivation and numerical solution of the equations for zero mach number combustion. *Combustion Science and Technology* **42** (3-4), 185–205.

Moureau, V., Bérat, C. & Pitsch, H. 2007 An efficient semi-implicit compressible solver for large-eddy simulations. *Journal of Computational Physics* **226** (2), 1256–1270.

Samtaney, R., Pullin, D. I. & Kosović, B. 2001 Direct numerical simulation of decaying compressible turbulence and shocklet statistics. *Physics of Fluids* **13** (5), 1415–1430.

Schardin, H 1957 High frequency cinematography in the shock tube. *The Journal of Photographic Science* **5** (2), 17–19.

Toro, E. F. & Vázquez-Cendón, M. E. 2012 Flux splitting schemes for the Euler equations. *Computers & Fluids* **70**, 1–12.

Zółtak, J. & Drikakis, D. 1998 Hybrid upwind methods for the simulation of unsteady shock-wave diffraction over a cylinder. *Computer Methods in Applied Mechanics and Engineering* **162**, 165–185.